frontiers in Materials

TYPE Original Research
PUBLISHED 03 September 2026
DOI 10.3389/fmats.2026.1912625

Evaluation of mechanical properties and durability of nanolime synthesized by an anion-exchange method for the consolidation of Dazu Rock Carvings

Zeyi Hao[1], Shuo Wang[1], Wengang Zhang[1]*, Andrea Galli[2], Bin Ma[1], Yanmei Zhang[1] and Yalin Cai[3]

[1]School of Civil Engineering, State Key Laboratory of Safety and Resilience of Civil Engineering in Mountain Area, College of Aerospace Engineering, Chongqing University, Chongqing, China, [2]The Department of Civil and Environmental Engineering, Politecnico di Milano, Milan, Italy, [3]Chongqing Cultural-Relics and Archaeology Research Institute, Chongqing, China

Check for updates

OPEN ACCESS

EDITED BY
Jingshou Liu,
China University of Geosciences Wuhan, China

REVIEWED BY
Ebrahim Sharifi Teshnizi,
Ferdowsi University of Mashhad, Iran
Indhumathi S.,
Sri Ramakrishna Engineering College, India

*CORRESPONDENCE
Wengang Zhang,
zhangwg@cqu.edu.cn

RECEIVED 18 June 2026
REVISED 12 July 2026
ACCEPTED 05 August 2026
PUBLISHED 03 September 2026

CITATION
Hao Z, Wang S, Zhang W, Galli A, Ma B, Zhang Y and Cai Y (2026) Evaluation of mechanical properties and durability of nanolime synthesized by an anion-exchange method for the consolidation of Dazu Rock Carvings. *Front. Mater.* 13:1912625. doi: 10.3389/fmats.2026.1912625

Introduction: Weathered sandstone at the Dazu Rock Carvings is susceptible to progressive loss of intergranular cohesion under repeated moisture fluctuations and salt crystallization. This study evaluated a compatible nanolime treatment designed to enhance the mechanical resistance of weathered sandstone while preserving its visual appearance and pore connectivity.

Methods: High-purity calcium hydroxide nanoparticles were synthesized via a one-step anion-exchange route. The synthesized nanolime and treated sandstone were characterized and evaluated using X-ray diffraction (XRD), transmission electron microscopy coupled with energy-dispersive spectroscopy (TEM/EDS), colorimetry, porosity and permeability measurements, uniaxial compressive strength (UCS) testing, nanoindentation mapping, accelerated wetting-drying and hygrothermal-salt aging tests, and in situ Leeb hardness monitoring.

Results: The synthesized nanolime consisted predominantly of hexagonal portlandite platelets approximately 50–100 nm in size, with no detectable chloride-containing crystalline by-products under the applied characterization conditions. Nanolime treatment increased the mean UCS from 37.35 to 47.00 MPa while causing negligible changes in color, porosity, and permeability. Following accelerated aging, nanolime-treated specimens retained higher hardness and elastic modulus than both untreated specimens and those treated with traditional lime water. Field monitoring further showed rapid recovery of surface hardness within 24 h after treatment, followed by continued strengthening over 100 days in selected weathered zones.

Discussion: These results demonstrate that anion-exchange-derived nanolime provides mineral-compatible reinforcement while maintaining the visual and hydro-physical characteristics of weathered sandstone. Longer-term field monitoring and direct assessment of carbonation depth are still required to establish its long-term durability and service-life performance.

KEYWORDS
anion-exchange synthesis, Dazu Rock Carvings, nanolime, rock conservation, sandstone consolidation

1 Introduction

Protection of cultural relics is not only a respect for history, but also a responsibility for cultural inheritance, social development, and the future of the nation. The importance and significance of protecting rock cultural relics, especially the rock cave temples, are becoming increasingly important. Sandstone cultural heritage, exemplified by the Dazu Rock Carvings in China, has undergone progressive deterioration due to long-term exposure to physical, chemical, and biological weathering mechanisms (He et al., 2014; Smith et al., 2011; Dehestani et al., 2020; Khanlari and Abdilor, 2015; Goudie and Viles, 1997; Mudronja et al., 2021; Aslan et al., 2001; Schuster et al., 1994; Onofri et al., 2014; Parvin et al., 2024; Wang et al., 2025a; Lin et al., 2024; Liu Y. et al., 2026; Guo et al., 2026). Among these, the Beishan Cliff Sculptures is particularly representative due to its exquisite carvings and complex micro-climatic exposure, making it a critical focus for this study (Sun, 2024). As illustrated in Figure 1, the site exhibits a variety of decay features. The loss of intergranular cohesion manifests as powdering, scaling, and granular disintegration, ultimately leading to structural instability and the gradual obliteration of carved details (Hanna et al., 1998; Wang et al., 2023). Consequently, the development of effective consolidation materials that can restore mechanical integrity while maintaining physicochemical compatibility with the original rock matrix has become a critical priority for heritage conservation.

Lime-based consolidants are theoretically suitable for sandstone conservation because of their chemical affinity with mineral substrates (Lanas and Alvarez, 2003). However, the conservation of weathered sandstone carvings imposes stricter requirements than simple chemical compatibility: the consolidant must penetrate fine pore-crack networks, restore intergranular cohesion, avoid secondary salt damage, and preserve surface appearance and vapor exchange. Traditional limewater is constrained by low solubility and insufficient penetration, and may introduce deleterious saline by-products that trigger destructive stress cycles within the pore network (Miller and Witt, 2002; Dai et al., 2010; Skoulikidis et al., 2005; Cultrone et al., 2007). Although advanced sol-gel or microemulsion techniques can improve morphological control, their application is often limited by high cost and difficult-to-remove surfactants (Daniele and Taglieri, 2012). In this context, high-purity nanolime synthesized through an anion-exchange resin method provides a promising route because it can reduce salt-related impurities while producing nanoscale calcium hydroxide particles (Taglieri et al., 2016; Taglieri et al., 2017a; Del Re, 2015; Taglieri et al., 2019). Nevertheless, previous studies on nanolime prepared by this route have mainly focused on mural pigment layers and lime mortars (Han et al., 2022; Otero et al., 2018; Wu et al., 2026). Its effectiveness for structurally reinforcing weathered sandstone carvings, where deeper penetration, surface-layer cohesion, and durability under moisture-salt cycling are essential, remains insufficiently understood.

In addition to the development of consolidants, previous studies have established a range of methods for evaluating treatment performance. Water absorption, porosity, permeability, and uniaxial compressive strength (UCS) tests are commonly used to characterize hydro-physical compatibility and macroscopic strengthening effects (Tang et al., 2018; İnce and Fener, 2016; Wang et al., 2026; Dai et al., 2020; Zhang et al., 2026; Zheng et al., 2023; Zheng and Baudet, 2024; Ren et al., 2026; Liu G. et al., 2026). Studies of weathered sandstone under wetting-drying and hygrothermal-salt exposure have further related mechanical deterioration to pore-scale loosening, microcrack propagation, and localized loss of intergranular cohesion (Zheng et al., 2022; Li et al., 2025; Hong et al., 2024). Nanoindentation mapping provides a complementary means of resolving the spatial distributions of hardness and elastic modulus in near-surface regions. However, existing studies have not yet established how anion-exchange nanolime reinforces weathered sandstone carvings across different length scales. In particular, conventional bulk measurements cannot determine the continuity of the reinforced surface layer or quantify the local mechanical response of mineral grains and intergranular contacts, while the durability of this treatment under coupled moisture and salt deterioration and its field applicability remain insufficiently understood. A multiscale evaluation method integrating physicochemical compatibility, macroscopic mechanical testing, nanoindentation mapping, accelerated aging, and field validation is therefore required.

In this paper, high-purity nanolime was synthesized using a surfactant-free anion-exchange method and applied to sandstone from the Dazu Rock Carvings. The nanolime was characterized by XRD and TEM, and its compatibility with sandstone was assessed by colorimetry, porosity, and permeability measurements. Reinforcement was evaluated by combining UCS testing with nanoindentation mapping, allowing bulk strength and the spatial micromechanical integrity of the near-surface layer to be examined within the same framework. Wetting-drying and hygrothermal-salt aging tests were then used to assess durability, followed by an *in-situ* field trial at the Beishan Cliff Sculptures. This approach links salt-minimized nanolime synthesis with multiscale mechanical evidence and field evaluation, with nanoindentation mapping providing the key local-scale assessment of reinforcement continuity and weathering resistance.

2 Materials and methods

The methodology of this study was organized into three main stages: material preparation, laboratory evaluation, and field validation. Sandstone specimens were first prepared from the Dazu Rock Carvings, followed by nanolime synthesis through a one-step anion-exchange route and characterization by TEM/EDS/HAADF and XRD. The untreated, traditional lime-water-treated, and nanolime-treated specimens were then evaluated through compatibility, mechanical performance, accelerated aging, and nanoindentation tests. Field applicability was further verified by *in-situ* Leeb hardness monitoring at representative weathered zones of the Beishan Cliff Sculptures. The overall methodological workflow is shown in Figure 2.

2.1 Experimental materials and instruments

The specimens used in this study were sandstone samples collected from the host rock of the Dazu Rock Carvings. To avoid anthropogenic damage and ensure the representativeness of the

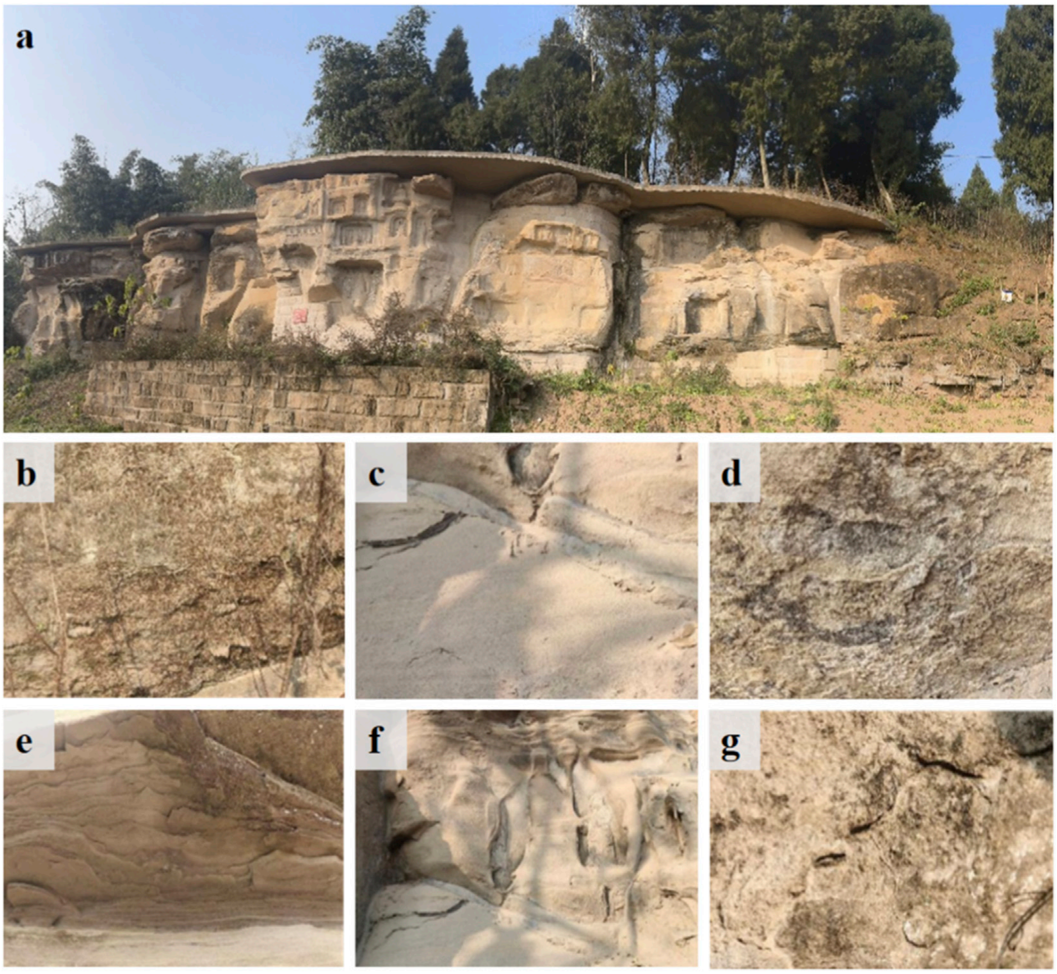

FIGURE 1
Typical weathering types of sandstone at the Dazu Rock Carvings: **(a)** overall panorama of the Beishan Cliff Sculptures; **(b)** granular disintegration and surface powdering; **(c)** longitudinal fissure; **(d)** biological crusts; **(e)** severe delamination showing characteristic bedding planes; **(f)** deep disintegration; **(g)** network of intersecting micro-cracks.

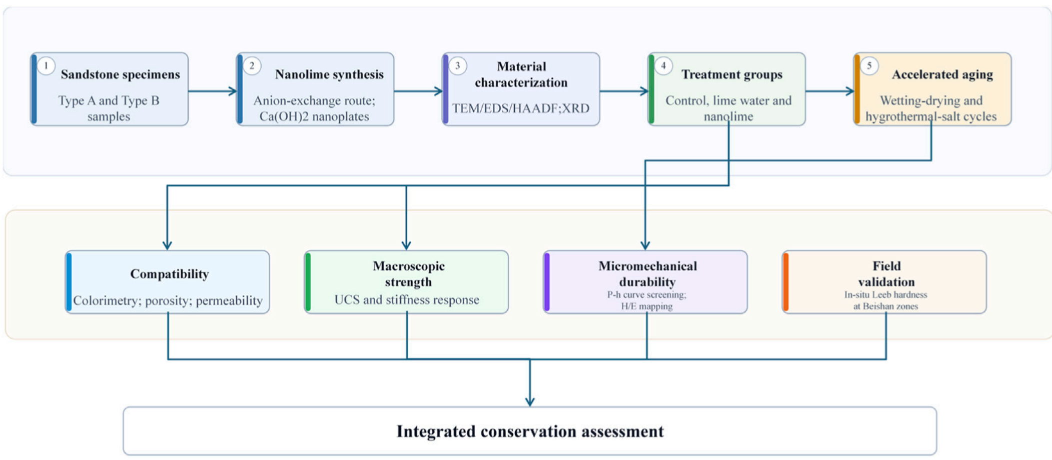

FIGURE 2
Methodological workflow for evaluating nanolime consolidation of weathered sandstone at the Dazu Rock Carvings.

FIGURE 3
Experimental instruments and samples for distinct testing phases.

specimens, rock blocks characterized by structural integrity, absence of macroscopic fissures, uniform mineralogical composition, and sufficient dimensions were prioritized during field selection, followed by laboratory core drilling. To ensure the consistency of experimental results, all specimens were extracted from the same rock mass. Two types of standardized specimens, designated as Sample A and Sample B, were prepared, as illustrated in Figure 3: eight cylindrical specimens (Type A) with a diameter of 2.5 cm and a length of 5 cm; and six cubic specimens (Type B) with a side length of 1 cm and a thickness of 0.5 cm.

High-purity nanolime was synthesized using analytical-grade calcium chloride dihydrate ($CaCl_2{\cdot}2H_2O$) as the calcium source and a strong base anion-exchange resin as the hydroxide source. Deionized water was employed as the reaction medium, and isopropanol was used to prepare the final nanoparticle dispersion. For comparison, traditional lime water was prepared from analytical-grade $Ca(OH)_2$. All consolidation tests were performed on sandstone samples obtained from the host rock of the Beishan Cliff Sculptures at the Dazu Rock Carvings.

A series of analytical techniques was employed to characterize the materials and evaluate their performance on the stone substrates. The analytical workflow and associated experimental setups are depicted in Figure 3. The morphology and elemental distribution of the synthesized nanolime were examined using TEM equipped with energy-dispersive X-ray spectroscopy (EDS) and a high-angle annular dark-field (HAADF) detector. Phase purity was determined by XRD. To assess aesthetic compatibility, a portable spectrophotometer was used to monitor color changes on the stone surface, the accuracy of which has been validated in prior studies (Han et al., 2022; Rodriguez-Navarro et al., 2013). Physical compatibility was evaluated through porosity and permeability tests, while macroscopic mechanical improvement was measured using a universal testing machine for UCS testing.

For durability assessment, treated samples were subjected to accelerated hygrothermal-salt and wetting-drying cycles in environmental chambers. After aging-induced mechanical deterioration, a nano-indentation system was utilized to measure surface hardness and elastic modulus, thereby evaluating the micromechanical resistance and stability of the reinforced layer.

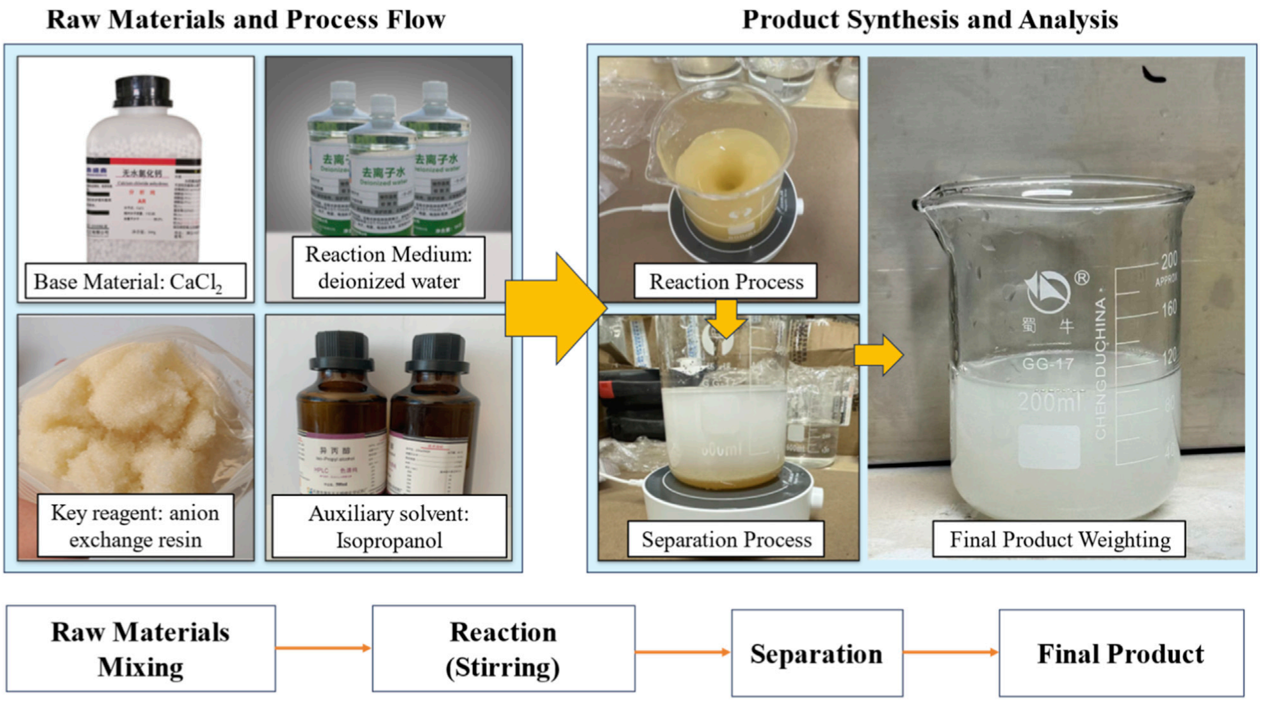

FIGURE 4
Preparation process of nanolime.

2.2 Preparation and characterization of reinforcement materials

The preparation of nanolime using the anion-exchange resin method is illustrated in Figure 4. For the synthesis, 1.19g of $CaCl_2 \cdot 2H_2O$ was dissolved in 80 mL of deionized water under constant stirring at 1,500 rpm to form a precursor solution. Subsequently, 15 g of a strong base anion-exchange resin (quaternary ammonium type) was introduced into the solution at room temperature and atmospheric pressure. This initiated the exchange between chloride ions Cl^- in the solution and hydroxide ions OH^- from the resin, as described by the following reaction:

$$CaCl_2 + 2(R - OH) \rightarrow Ca(OH)_2 \downarrow +2(R - Cl)$$

where R represents the high-molecular-weight polymer matrix of the anion-exchange resin.

Due to the resulting supersaturation, pure $Ca(OH)_2$ nanoparticles precipitated rapidly, causing the solution to turn from transparent to a turbid, milky-white suspension. The reaction was terminated after 10 min of stirring, and the resin beads were separated from the colloidal suspension by filtration.

To verify the completion of the ion exchange, the residual Cl^- concentration in the supernatant was measured using an Ion Chromatograph. The concentration decreased from an initial 7.66 g/L to 0.11 g/L, representing a removal efficiency of approximately 98.6%. Finally, 40 mL of the resulting suspension was extracted and mixed with 40 mL of isopropanol to obtain a nanolime consolidant with a $Ca(OH)_2$ concentration of 3.35 g/L in a 1:1 (v/v) water/isopropanol dispersion.

The nanolime concentration and solvent system were selected based on previous conservation studies. A 3.35 g/L $Ca(OH)_2$ suspension in a 1:1 (v/v) water/isopropanol mixture was adopted to ensure sufficient penetration capacity while avoiding excessive surface accumulation and pore blockage (Han et al., 2022; Otero et al., 2020; Busschots et al., 2025).

The physicochemical properties of the synthesized nanolime were characterized to assess the quality of the material. Particle morphology and size were examined using TEM and HAADF imaging. For TEM observation, the nanolime dispersion was diluted with isopropanol and dropped onto carbon-coated copper grids. Elemental composition and distribution were analyzed by EDS coupled with the TEM system. In addition, the crystalline phase and purity of the dried powder were determined by XRD to identify the mineralogical composition and detect any possible impurities.

Regarding the control group, traditional lime water was prepared from analytical-grade $Ca(OH)_2$. To mitigate potential surface whitening effects and ensure physicochemical compatibility with the substrate, a low-concentration solution of 0.5 g/L was employed, which is significantly below the saturation point of calcium hydroxide at room temperature (approximately 1.7 g/L).

The concentration difference between the traditional lime water and nanolime treatments reflects practical conservation constraints rather than an equal-mass comparison. The lime-water concentration was deliberately kept low to reduce the risk of surface whitening and pore blockage, whereas the nanolime suspension was used at the concentration that remained stable and applicable in the water/isopropanol carrier. Therefore, the comparison should be interpreted as a comparison between two practically applicable treatment protocols. The possible influence of Ca(OH)2 dosage

TABLE 1 Summary of consolidant mixtures, curing conditions, aging exposures, and tests conducted.

Group	Treatment	Curing
Control	Untreated sandstone	No consolidant; same specimen preparation
Traditional	0.5 g/L	Three brushing cycles; 20 ℃ ± 2 ℃ and 50% ± 5% RH curing for 1 week
Nanolime	3.35 g/L	Three brushing cycles; 20 ℃ ± 2 ℃ and 50% ± 5% RH curing for 1 week

on the observed performance difference is acknowledged as a limitation.

2.3 Consolidation treatment

The consolidation of sandstone specimens was performed using the brushing method. The specimens were divided into two treatment groups: one treated with the low-concentration traditional lime water (0.5 g/L) and the other with the nanolime suspension (3.35 g/L).

The concentration difference between the two consolidants was intentionally retained to reflect practical conservation constraints rather than an equal-mass comparison: the traditional lime water was kept at a low concentration to avoid surface whitening and pore blocking, whereas the nanolime suspension was prepared at the concentration that remained stable and applicable in the water/isopropanol carrier. Therefore, the comparison evaluates the performance of the two practically applicable treatment protocols, while the influence of Ca(OH)2 dosage is acknowledged as a limitation for direct material-to-material comparison.

The application procedure was as follows:

1. During each treatment cycle, the consolidant was uniformly brushed onto the entire surface of each cylindrical Type A specimen at an application rate of 5 mL per 100 cm2. Given the specimen diameter of 2.5 cm and length of 5 cm, the total surface area was approximately 49.1 cm^2, corresponding to about 2.45 mL of consolidant per specimen per cycle. Three application cycles were used to ensure repeated wetting and sufficient consolidant uptake while avoiding visible surface accumulation.
2. The treated samples were subsequently dried in a controlled laboratory environment at ambient temperature and pressure for 24 h. To verify complete desiccation and quantify the dry matter uptake of the consolidants, the specimens were weighed before and after each application cycle. This process was repeated three times.
3. Finally, all consolidated specimens were cured for 1 week in a controlled environment (temperature of 20°C ± 2 °C and relative humidity of 50% ± 5%) to ensure sufficient carbonation and stabilization prior to subsequent performance evaluations.

To make the experimental design more explicit, the consolidant mixtures, curing conditions, aging exposures, and specific tests conducted for each treatment group are summarized in Table 1.

2.4 Colorimetric analysis

To assess the aesthetic impact of the consolidants, colorimetric measurements were performed on the sandstone samples before and after treatment. Color parameters were recorded using a portable spectrophotometer and expressed in the CIElab color space (Otero et al., 2018).

For each treatment group (Traditional Lime and Nanolime), measurements were conducted on duplicate stone samples. To ensure statistical representativeness and account for the natural heterogeneity of the sandstone, five independent points were measured on each sample surface. The mean values of L^*, a^*, and b^* were then calculated for each group. The total color difference ($\Delta E^*{}_{ab}$) induced by the consolidation treatment was quantified using the following equation:

$$\Delta E^*_{ab} = \sqrt{(\Delta L^*)^2 + (\Delta a^*)^2 + (\Delta b^*)^2}$$

$$\Delta L^* = L^*_2\text{-}L^*_1\ , \Delta a^* = a^*_2\text{-}a^*_1, \Delta b^* = b^*_2\text{-}b^*_1$$

Where L^*, a^*, and b^* represent lightness, the red–green chromatic coordinate, and the yellow–blue chromatic coordinate in the CIElab color space, respectively. The subscripts 1 and 2 denote the values measured before and after treatment, respectively; for example, $L^*{}_1$ and $L^*{}_2$ refer to the lightness values before and after consolidation. This standardized approach was used to evaluate whether the nanolime treatment maintained the visual integrity of the sandstone substrate.

2.5 Evaluation of consolidation performance

To evaluate the permeability and mechanical performance of the synthesized nanolime for stone grotto conservation, a comprehensive experimental program was designed. The study included comparative analyses with traditional lime treatment and untreated control samples. Specimens were divided into six experimental groups (1a–1f) for durability assessment. Considering the local environmental conditions at the Dazu Rock Carvings—characterized by high rainfall and saline water distribution—two accelerated aging protocols were adopted: wetting-drying cycles and hygrothermal-salt cycles (Wang and Hua, 1998; Jiahang et al., 2022; Yang et al., 2025).

TABLE 2 Experimental design for evaluating consolidation effectiveness and durability of nanolime-treated sandstone.

Group	Reinforcement strategy	Consolidation effectiveness assessment (Type A)	Consolidation durability assessment (Type B)
	I: Hygrothermal-salt cycles		
1a	Control	Porosity, permeability, UCS	Nanoindentation
1b	Traditional	Porosity, permeability, UCS	Nanoindentation
1c	Nanolime	Porosity, permeability, UCS	Nanoindentation
	II: Wetting-drying cycles		
1d	Control	Porosity, permeability, UCS	Nanoindentation
1e	Traditional	Porosity, permeability, UCS	Nanoindentation
1f	Nanolime	Porosity, permeability, UCS	Nanoindentation

For the wetting-drying cycles, the specimens were immersed in water for 24 h and then dried for 24 h at 30 °C and 50% relative humidity; this sequence was defined as one complete wetting–drying cycle. For the hygrothermal-salt cycles, the specimens were immersed in saturated sodium sulfate solution for 24 h and then dried for 24 h under the same environmental condition of 30 °C and 50% relative humidity; this sequence was defined as one complete hygrothermal–salt cycle. The 20-day aging protocol was selected as a moderate accelerated durability test based on previous stone-conservation studies. For comparison, Rodriguez-Navarro et al. (2013) used 14 salt crystallization cycles to assess nanoconsolidant-treated stone, whereas Barnoos et al. (2022) used 70 freeze-thaw cycles to evaluate consolidated limestone durability.

Within each group, specimens were further divided into two types based on the subsequent tests. Specimens designated as Type A were subjected to helium pycnometry and uniaxial compression testing to measure their macroscopic physical properties, including porosity, permeability, and UCS. For UCS testing, two Type A specimens were tested for each treatment condition (untreated, traditional lime water and nanolime). Because the available heritage sandstone material was limited, these UCS data were used for descriptive comparison of treatment response rather than for inferential statistical testing. These metrics were used to evaluate the stones' breathability and the overall consolidation effectiveness. Meanwhile, Type B specimens were first subjected to a 20-day accelerated aging period, followed by nano-indentation testing. This was performed to assess the micromechanical evolution, specifically the retention of surface hardness and elastic modulus of the treated layer under weathering stress (Liu et al., 2016; Yang et al., 2024; Gupta et al., 2020).

After this overall treatment, the detailed allocation of the six experimental groups is presented in Table 2. This table distinguishes the specimens used for consolidation effectiveness assessment from those used for durability assessment, thereby clarifying how Type A and Type B samples were assigned to macroscopic tests and post-aging nanoindentation tests, respectively.

3 Results

3.1 Synthesis and characterization of nanolime

The morphology, elemental distribution, and crystalline phase of the synthesized product were characterized to confirm the successful preparation of nanolime by means of the anion exchange method.

TEM and HAADF imaging revealed that the synthesized particles exhibit a well-defined hexagonal platelet morphology, characteristic of portlandite crystals (Figures 5a,b,e,f) (Han et al., 2022; Stepkowska et al., 2002). The particles exhibit a relatively narrow size distribution, predominantly ranging from 50 to 100 nm, demonstrating that the anion-exchange process effectively restricts grain growth at the nanoscale. EDS mapping showed a homogeneous distribution of calcium Ca and oxygen O throughout the hexagonal platelets, confirming the chemical uniformity of the calcium hydroxide nanoparticles (Figures 5c,d,g,h).

The phase composition and purity of the product were further examined by XRD (Figures 5i,j). The diffraction pattern displayed sharp, intense Bragg reflections, indicating a high degree of crystallinity (Pope, 1997). All detectable peaks were perfectly indexed to the standard hexagonal phase of calcium hydroxide (De Matos et al., 2022). Notably, no characteristic peaks of calcite or chloride-bearing by-products were detected, indicating that the synthesis yielded high-purity nanolime, effectively prevented premature carbonation, and avoided soluble chloride residues that could otherwise crystallize during moisture fluctuations and accelerate deterioration.

3.2 Colorimetric results and aesthetic compatibility

Aesthetic compatibility is a fundamental requirement for materials used in cultural heritage conservation, as treatments must not alter the intrinsic visual appearance of the artwork. Table 3 presents the chromatic coordinates (L^*, a^*, b^*) and the calculated total color differences ($\Delta E^*{}_{ab}$) for the sandstone samples before and after consolidation.

10.3389/fmats.2026.1912625

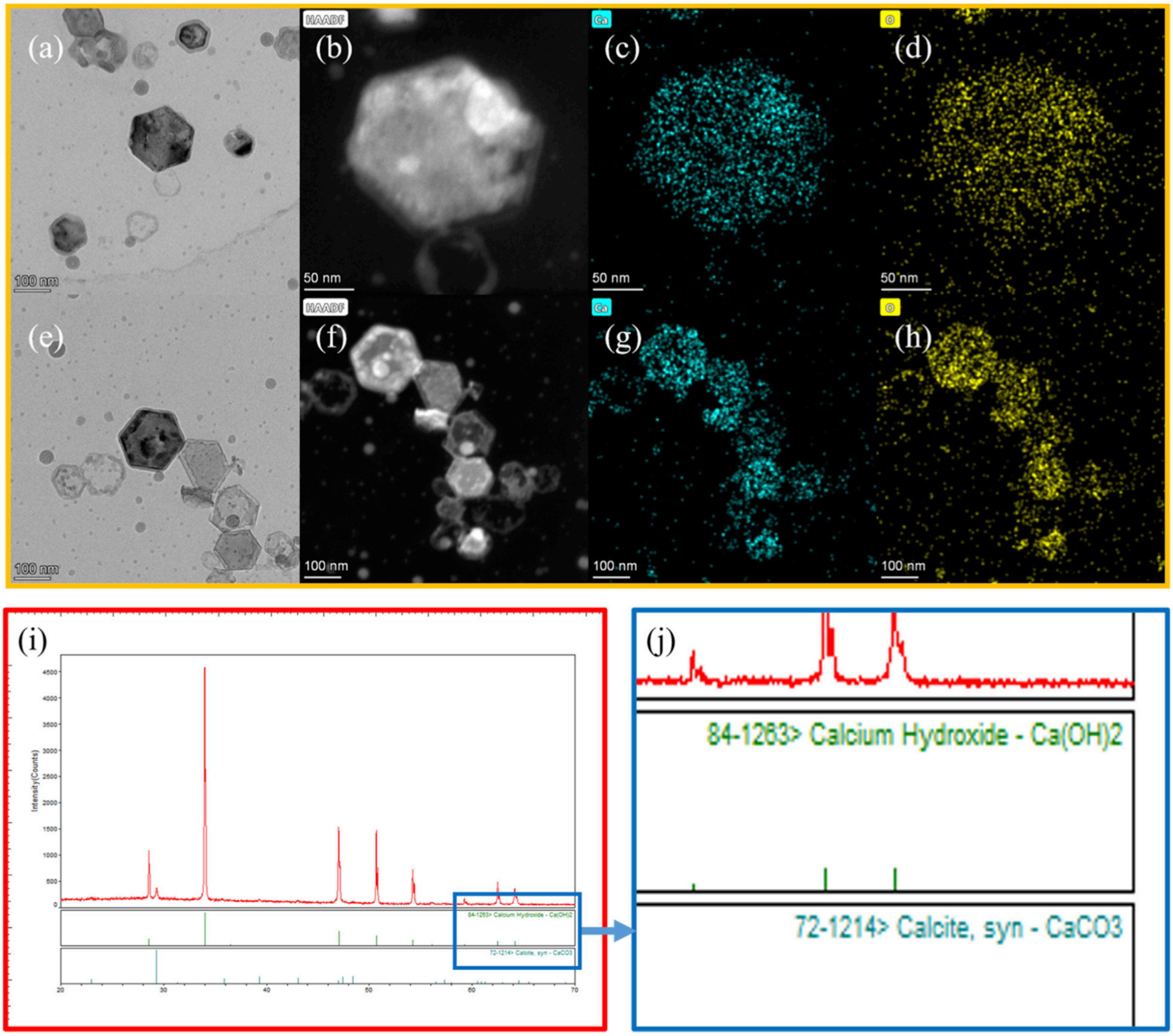

FIGURE 5
Microstructural and phase characterization of the calcium hydroxide nanoplates. **(a,e)** Bright-field TEM images showing hexagonal morphology. **(b,f)** HAADF-STEM images. **(c,d)** and **(g,h)** EDS elemental mapping of Ca and O, respectively. **(i)** XRD pattern of the sample. **(j)** Detailed comparison with standard PDF cards for $Ca(OH)_2$ and $CaCO_3$.

TABLE 3 **Colorimetric parameters and chromatic changes of samples treated with traditional lime and nanolime.**

Treatment group	Sample ID	L*	a*	b*	ΔL*	Δa*	Δb*	ΔE^*_{ab}
Control (untreated)	Standard	62.81 ± 1.05	2.19 ± 0.35	5.79 ± 0.72	—	—	—	—
Traditional lime	A1	62.16 ± 0.38	2.11 ± 0.52	6.38 ± 0.51	−0.65	−0.08	0.59	0.88
(Sample A)	A2	62.84 ± 0.20	2.61 ± 0.58	5.83 ± 0.47	0.04	0.42	0.05	0.43
	Mean	62.50 ± 0.49	2.36 ± 0.36	6.11 ± 0.39	−0.31 ± 0.49	0.17 ± 0.36	0.32 ± 0.39	0.66 ± 0.32
Nanolime	B1	62.98 ± 0.43	2.49 ± 0.43	5.02 ± 0.40	0.17	0.30	−0.76	0.83
(Sample B)	B2	61.99 ± 1.00	2.58 ± 0.56	5.66 ± 0.68	−0.81	0.39	−0.12	0.91
	Mean	62.49 ± 0.70	2.54 ± 0.07	5.34 ± 0.45	−0.32 ± 0.70	0.34 ± 0.07	−0.44 ± 0.45	0.87 ± 0.06

The untreated control samples served as the reference, with mean chromatic values of $L^* = 62.81$ (lightness), $a^* = 2.19$ (red-green component), and $b^* = 5.79$ (yellow-blue component). After treatment with traditional lime water (Group A), the samples showed a minimal color shift, with an average total color difference (ΔE^*_{ab}) of 0.66. This change was primarily attributed to a slight decrease in lightness ($\Delta L = -0.31$) and a marginal increase in the yellow component ($\Delta b^* = 0.32$).

Similarly, the samples treated with the synthesized nanolime exhibited excellent color stability. The mean ΔE^*_{ab} for the nanolime group was calculated at 0.88, with individual samples ranging between 0.84 and 0.91. While the nanolime treatment resulted in a slight negative shift in the b axis ($\Delta b^* = -0.44$), indicating a negligible reduction in yellowness, the overall lightness and chromaticity remained very close to the standard.

According to the commonly used aesthetic compatibility criterion for conservation treatments, a total color difference below 3 is considered hardly perceptible, a value between 3 and 6 is perceptible but acceptable, and a value above 6 is unacceptable (Han et al., 2022). In the present study, both the traditional lime water group (mean $\Delta E^*_{ab} = 0.66$) and the nanolime group (mean $\Delta E^*_{ab} = 0.88$) were well below the perceptibility threshold of 3. Therefore, the color variations induced by both treatments can be regarded as visually negligible, confirming that the synthesized nanolime satisfies the aesthetic compatibility requirement for sandstone conservation.

3.3 Effect on porosity and permeability

The impact of the consolidation treatments on the pore structure and transport properties was evaluated by comparing the porosity and gas permeability of each group before and after reinforcement. This comparison was used not only to quantify pore-volume variation, but also to assess whether consolidation altered the connected transport network that controls moisture exchange in weathered sandstone.

As illustrated in Figure 6, both materials induced only marginal changes to the physical structure of the sandstone. For the traditional reinforcement group, the average porosity decreased from 14.0% to 13.9%, representing a relative reduction of 0.71%. In comparison, the nanolime reinforcement group started with a higher initial porosity of 14.5%, which shifted to 14.4% after treatment, corresponding to a relative decrease of 0.69%. The very small reduction in open porosity indicates that neither treatment produced extensive pore filling at the specimen scale, which is a prerequisite for maintaining vapor exchange in heritage sandstone. Therefore, the porosity response is better interpreted as specimen-scale preservation of the pore network rather than pore densification. Because open porosity is a bulk volume-fraction parameter, this small change does not exclude localized deposition or contact-point strengthening; instead, it indicates that any modification was limited and did not develop into extensive pore occlusion.

The permeability data followed a similar trend of high retention. In the traditional reinforcement batch, the permeability declined from 2.5 mD to 2.4 mD, a relative reduction of 4.0%. For the nanolime reinforcement group, the permeability was maintained at 5.4 mD from an initial value of 5.5 mD, showing a slightly lower relative reduction of 1.8%. These data indicate that while both treatments result in a minimal loss of pore volume, the nanolime reinforcement demonstrates a marginally higher capacity for preserving the original gas transport properties of the sandstone. This permeability retention is especially relevant for exposed cliff carvings. In such environments, moisture exchange is unavoidable, and a consolidant that improves mechanical strength but severely reduces transport capacity would be unsuitable. Since gas permeability is governed more directly by pore-throat size, connectivity, constriction, and tortuosity than by total porosity alone, its high retention provides a more sensitive indication that the effective flow pathways remained largely continuous after treatment. It should also be noted that the two batches had different initial permeability values; therefore, the comparison is more rigorously based on the relative permeability retention within each group rather than on the absolute post-treatment values alone. From this perspective, the nanolime treatment showed a slightly better ability to preserve transport compatibility, achieving mechanical reinforcement without a substantial penalty in gas transport performance.

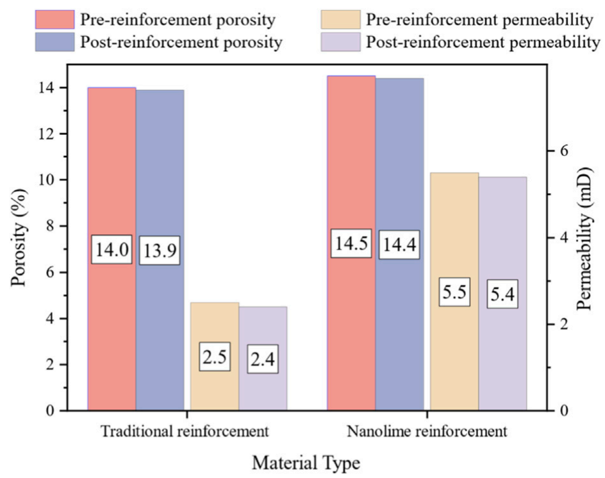

FIGURE 6
Porosity and Permeability evaluation of the samples treated with traditional lime and nanolime.

3.4 UCS results

The mechanical performance of the consolidants was quantitatively evaluated through UCS tests. The representative stress–strain curves, illustrated in Figure 7, demonstrate the influence of each treatment on the load-bearing capacity and deformation behavior of the sandstone. To quantify the strengthening effect, the reinforcement rate (η) was calculated using the following equation:

$$\eta = \frac{\left(\sigma_{after} - \sigma_{before}\right)}{\sigma_{before}} \times 100\%$$

where η is the compressive strength reinforcement rate; σ_{before} is the compressive strength of the sandstone before reinforcement, MPa; and σ_{after} is the compressive strength of the sandstone after reinforcement, MPa.

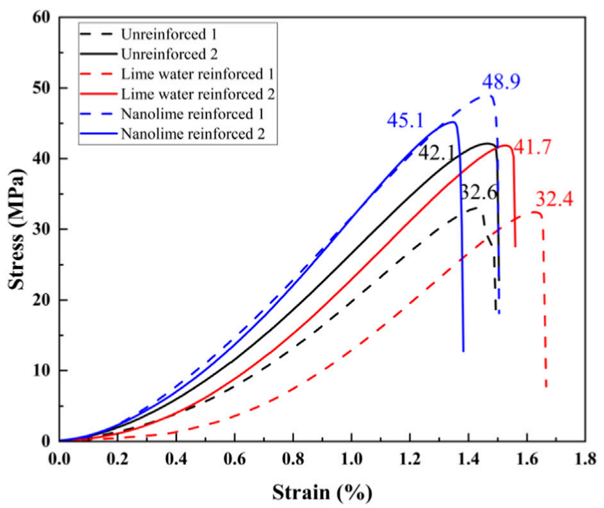

FIGURE 7
Stress-strain curves of unreinforced, lime water and nanolime treated specimens.

The peak compressive strengths of the unreinforced control specimens were 32.6 MPa and 42.1 MPa, giving an average baseline strength of 37.35 MPa. After treatment with traditional lime water, the peak stresses were 32.4 MPa and 41.7 MPa, with an average of 37.05 MPa. This corresponds to a negligible reinforcement rate of approximately −0.8%, indicating that traditional lime water did not improve the compressive resistance of the sandstone under the present treatment conditions. In contrast, the nanolime-treated specimens reached peak strengths of 45.1 MPa and 48.9 MPa, with an average of 47 MPa. The absolute UCS increase was therefore 9.65 MPa, corresponding to a reinforcement rate of 25.8%.

The UCS values measured in this study were compared with previously reported results for Dazu sandstone. Wang et al. (2025b) reported a dry-state UCS of 63.72 MPa for Dazu sandstone, which decreased to 24.7 MPa after saturation. Guo et al. (2025) reported a UCS of 62.2 ± 1.1 MPa for Dazu sandstone in a comparative study of grotto sandstones. The baseline UCS obtained in the present study (37.35 MPa) is lower than the dry-state values reported in these studies. This discrepancy may be related to differences in sampling location, lithological heterogeneity, bedding orientation, pore structure, cementation degree, moisture condition, specimen preparation, and testing protocol. Therefore, the published UCS values were used as comparative references rather than direct baselines for calculating the reinforcement effect.

Within the present experimental system, the comparison among treatment groups remains clear. Traditional lime water produced almost no change in UCS, whereas nanolime increased the average UCS from 37.35 MPa to 47 MPa. This result indicates that, despite the difference between the present baseline strength and previously reported values, nanolime provided a measurable strengthening effect under the same sample preparation and testing conditions.

Beyond peak strength, the nanolime treatment also increased stiffness. The linear elastic segment of the nanolime-treated stress-strain curves was steeper than those of both the untreated and lime-water-treated groups, indicating an increase in Young's modulus. Thus, nanolime improved both compressive resistance and elastic deformation resistance, whereas traditional lime water showed little strengthening effect.

3.5 Micromechanical properties and durability

To systematically evaluate the durability of the consolidation effect under simulated weathering conditions, nano-indentation tests were performed on the aged stone samples, with a total of 36 test points collected. The indentation points were arranged with a spacing of 10 μm between adjacent points to minimize potential interaction effects between neighboring measurements. Figures 8a–f presents representative load–displacement (P–h) curves from different experimental groups. For clarity, 12 representative curves are shown; missing data points were supplemented by values from adjacent valid locations.

The shape of these curves provides insight into the mechanical resistance and plastic deformation behavior of the surface layer. For samples subjected to wetting–drying cycles (Figures 8a–c) and hygrothermal–salt cycles (Figures 8d–f), the untreated control and traditional lime-treated specimens exhibited broad hysteresis loops with large maximum penetration depths, typically exceeding 1,000 nm. The curves for these groups were widely dispersed and frequently displayed pop-in events—sudden increases in displacement without a corresponding increase in load—indicating micro-cracking, void collapse, or structural loosening induced by weathering stress. These features show that the weathered surface after aging did not respond as a continuous elastic-plastic solid, but contained weak zones that collapsed progressively during indentation.

In sharp contrast, the load–displacement curves for the nanolime-treated samples were characterized by steep loading slopes and significantly reduced maximum penetration depths (typically < 400 nm) under the same peak load (Figures 8c,f). Moreover, the curves for the nanolime groups showed narrow dispersion, suggesting that the consolidation treatment formed a mechanically uniform layer that effectively mitigated the heterogeneity of the weathered sandstone surface. The reduced penetration depth under identical peak load directly indicates higher local hardness, while the overlap among repeated curves supports the reproducibility of the surface reinforcement effect.

Two representative abnormal curves were further extracted to clarify the relationship between curve-level instability and spatial mapping results (Figure 9). Point 13 (Figure 9a) is a typical pop-in response in the untreated specimen after wetting-drying cycles. The sudden displacement burst during loading indicates that the indenter triggered local instability beneath the contact area, which can be attributed to pore collapse, grain-boundary slip, or microcrack activation in the loosened weathered surface. This pop-in event explains why some indentation points in the untreated group could not provide a stable elastic-plastic response for reliable mapping. In contrast, point 34 (Figure 9b) is characterized by an abnormally large penetration depth in the traditional lime-water-treated specimen after hygrothermal-salt cycles. This excessive indentation depth indicates a highly compliant local zone, suggesting that salt-related damage and insufficient consolidation left a weak surface region even after lime-water treatment. Therefore,

10.3389/fmats.2026.1912625

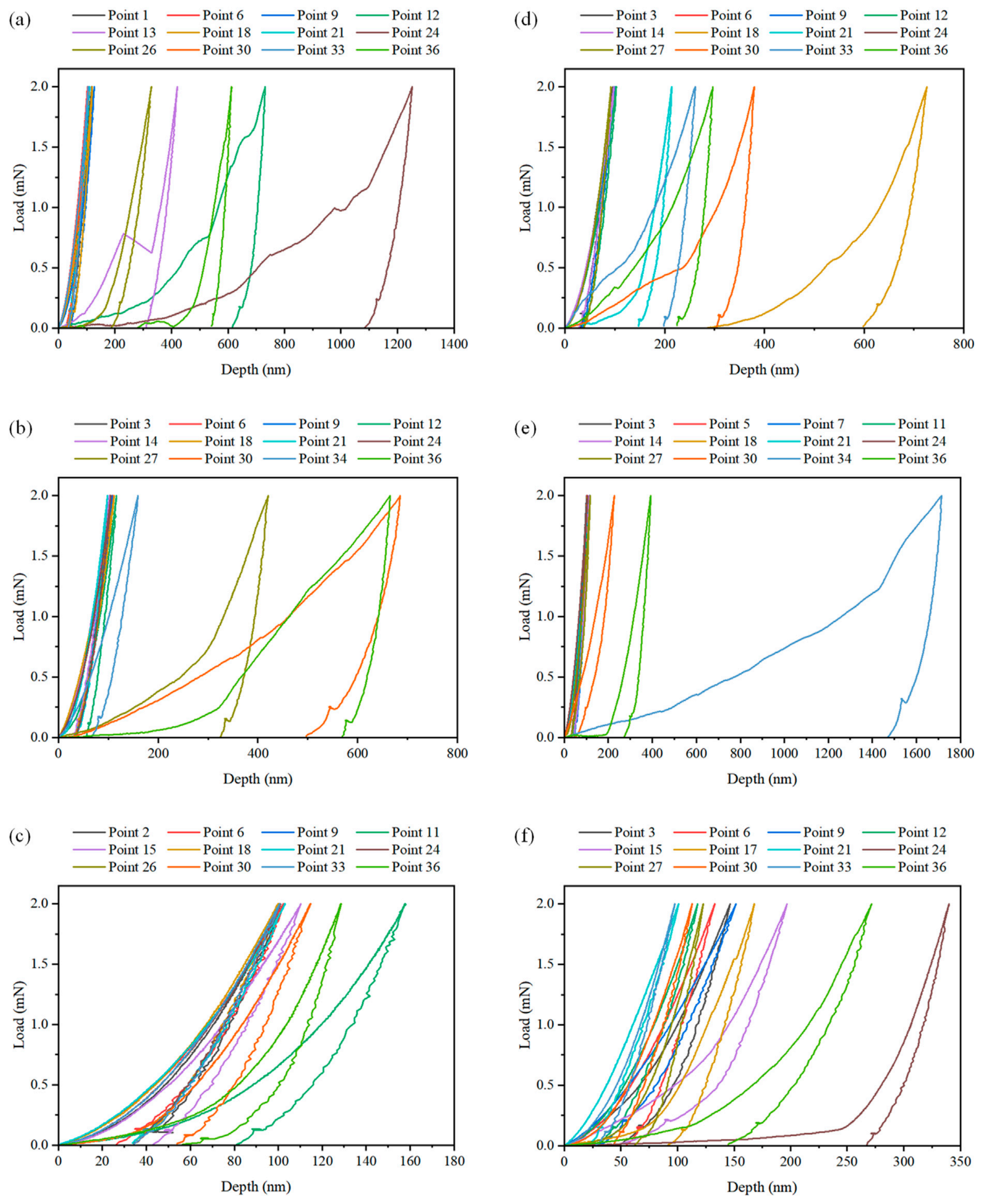

FIGURE 8
Typical load-displacement curves from nano-indentation tests. **(a–c)** Curves under wetting-drying cycles; **(d–f)** curves under hygrothermal-salt cycles.

point 13 and point 34 represent two different failure signatures: abrupt local collapse during loading and excessive penetration into a softened surface layer, respectively.

Based on the load-displacement data, hardness (H) and elastic modulus (E) were calculated using the Oliver–Pharr method to quantify the micromechanical properties of the treated surface layer. The spatial distributions of these properties are presented as color-coded maps in Figure 10, with corresponding statistical summaries provided in Table 4. In the statistical calculation, black regions in the mapping images were treated as invalid indentation points and

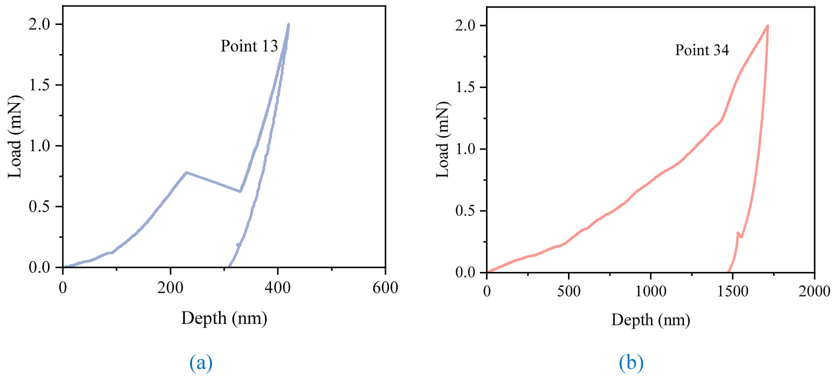

FIGURE 9
Representative abnormal nanoindentation load-displacement curves: **(a)** point 13 from the untreated specimen after wetting-drying cycles; **(b)** point 34 from the traditional lime-water-treated specimen after hygrothermal-salt cycles.

were excluded from the calculation of mean values and standard deviations, because these locations corresponded to failed contact, excessive surface loss, or unreliable load-displacement curves rather than valid mechanical responses of the intact material.

Under wetting-drying cycles (Figures 10a–c,g–i), the untreated control and traditional lime-treated samples exhibited significant surface instability. Their property maps were characterized by scattered black regions, indicating invalid test points where the indenter failed to contact a sound surface due to cyclic hydraulic stress. Quantitatively, the residual measurable areas in the control group showed low average values of $H = 5.85 \pm 5.06$ GPa and $E = 54.13 \pm 40.31$ GPa. Traditional lime treatment provided only marginal improvements ($H = 7.18 \pm 4.51$ GPa, $E = 66.85 \pm 32.26$ GPa). In contrast, the nanolime-treated sample (Figures 10c,i) maintained a dense and intact microstructure with negligible black voids. It exhibited significantly higher micromechanical integrity, with an average value of $H = 9.66 \pm 3.29$ GPa and $E = 92.05 \pm 21.77$ GPa, representing a substantial enhancement in surface cohesion. The contrast between scattered invalid regions and continuous colored zones demonstrates that the difference was not restricted to isolated indentation points, but reflected the spatial continuity of the treated surface layer.

A similar but more severe deterioration pattern was observed under hygrothermal-salt cycles (Figures 10d–f,j–l). Extensive black regions in the control and traditional lime-treated groups indicated massive material loss caused by salt crystallization pressure. For the untreated control group, the mechanical properties dropped to average values of $H = 5.35 \pm 5.17$ GPa and $E = 66.13 \pm 38.36$ GPa. Similarly, traditional lime water failed to provide effective protection, with measured values of $H = 6.72 \pm 4.01$ GPa and $E = 67.86 \pm 35.42$ GPa,indicating that the reinforcement was insufficient to counter the disruptive forces of salt crystallization. In contrast, the nano lime-treated sample (Figures 10f,l) presented a much more continuous surface with significantly higher and more stable average values of $H = 7.02 \pm 3.10$ GPa and $E = 73.68 \pm 24.37$ GPa. The preservation of measurable hardness and modulus under the more aggressive salt-containing cycle further indicates that the nanolime treatment retained its protective effect under coupled thermal, moisture, and crystallization stresses.

4 Discussion

To validate the laboratory results under real conservation conditions, a field trial was conducted on the northern cliff-carved sandstone surfaces of the Dazu Rock Carvings, where the rock mass is exposed to complex cliff-topography-controlled microenvironments, including windward-sunny and leeward-shaded zones (Wang and Hua, 1998; Jiahang et al., 2022; Zhao et al., 2024; Yang et al., 2025). Five representative monitoring points were selected to cover different initial weathering states and surface morphologies in Figure 11. Point 1 was located in a windward-sunny area with dense fine pore-cracks and slight surface powdering; Point 2 was also located in a windward-sunny area but was characterized mainly by small open fissures; Point 3 represented a severely weathered zone with relatively long and wide fractures and local granular disintegration; Point 4 was located in a leeward-shaded area with extremely fine pore-cracks and higher moisture retention; and Point 5 represented a leeward-shaded surface with medium-sized fissures and loose surface dust. Before treatment, the monitoring areas were gently cleaned and dried to reduce the influence of detached particles on consolidant penetration and hardness testing.

During field application, the nanolime consolidant was applied at a dosage of 0.5 mL per 10 cm^2 of treated surface. The application method was adjusted according to the local deterioration morphology: precision micro-injection using needle syringes was used for the fine pore-crack zones at Points 1 and 4; a rubber-head dropper was used for the small-fissure zone at Point 2; a 5 cm brush was used for the larger fractured area at Point 3; and a sterile medical disinfection brush was used for the medium-fissure and dust-cleaned surface at Point 5. *In-situ* Leeb hardness was measured at marked locations within each treated area before treatment, during the first 24 h after application, and again after 100 days. At each monitoring time, three repeated Leeb hardness measurements were performed at adjacent positions within the same marked area, and the mean value was used to represent the local surface mechanical response. This design allowed the field data to reflect both the short-term strengthening effect of nanolime and

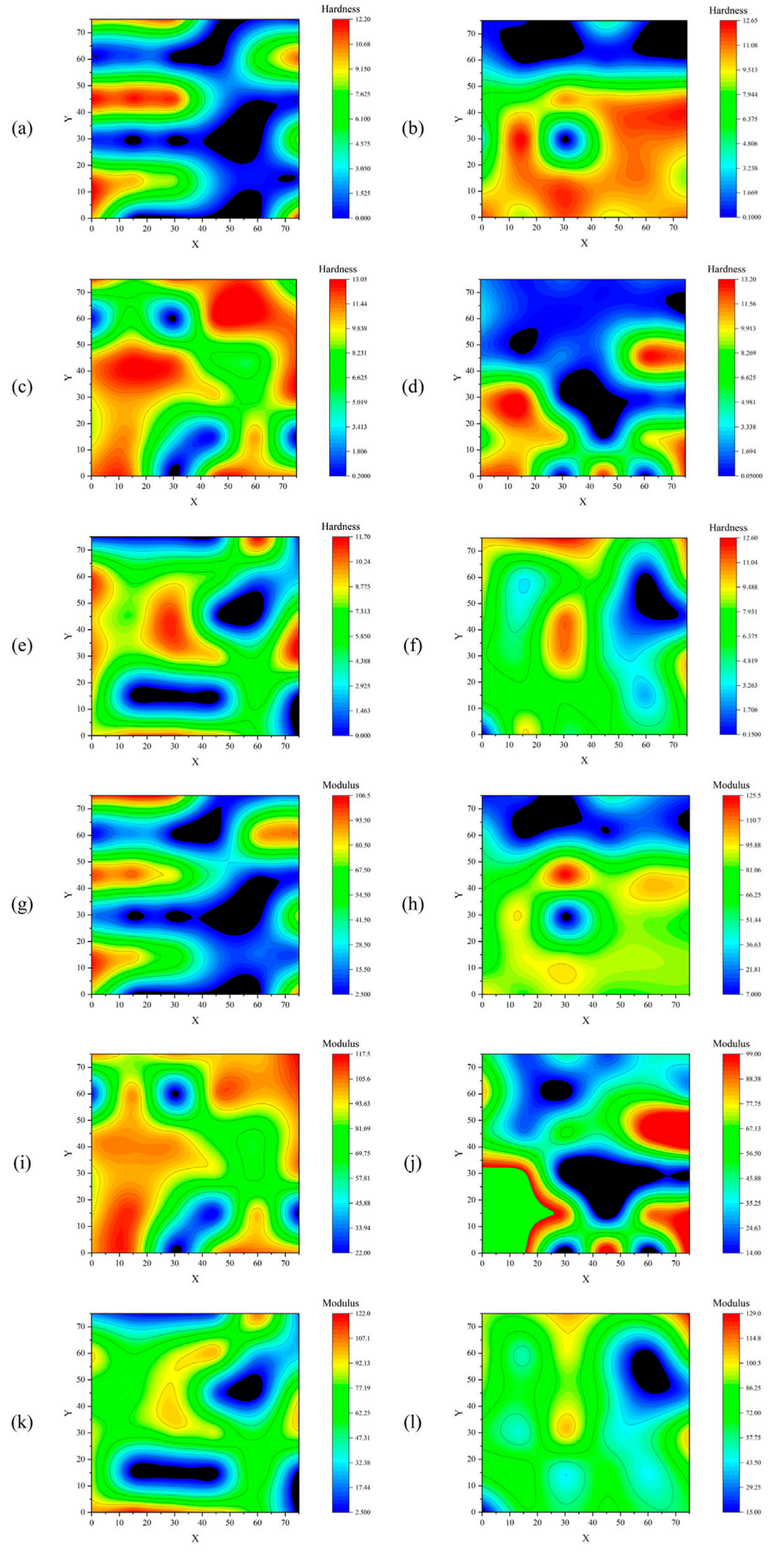

FIGURE 10
Nanomechanical hardness and elastic modulus mapping of the sandstone samples after various aging treatments. Hardness maps for samples subjected to **(a–c)** wetting-drying cycles and **(d–f)** salt weathering; Modulus maps for samples subjected to **(g–i)** wetting-drying cycles and **(j–l)** salt weathering. Within each group, **(a,d,g,j)** represent the untreated (unreinforced) samples, **(b,e,h,k)** represent those treated with traditional lime, and **(c,f,i,l)** represent those treated with nanolime.

TABLE 4 Statistical summary of micromechanical properties after environmental aging.

Environment	Treatment	Property	Mean value (GPa)	*SD* (GPa)
After wetting-drying cycles	Unreinforcement	*H*	5.85	5.06
		E	54.13	40.31
	Lime water reinforcement	*H*	7.18	4.51
		E	66.85	32.26
	Nanolime reinforcement	*H*	9.66	3.29
		E	92.05	21.77
After hygrothermal-salt cycles	Unreinforcement	*H*	5.35	5.17
		E	66.13	38.36
	Lime water reinforcement	*H*	6.72	4.01
		E	67.86	35.42
	Nanolime reinforcement	*H*	7.02	3.1
		E	73.68	24.37

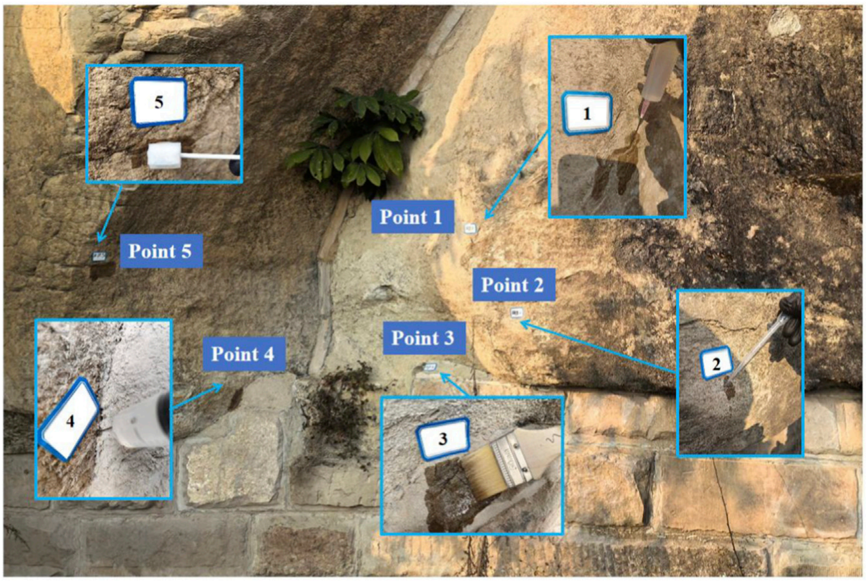

FIGURE 11
Spatial distribution of the selected monitoring points on the Beishan Cliff Sculptures at the Dazu Rock Carvings.

the influence of initial weathering state, application method, and cliff-surface microenvironment on the 100-day hardness evolution.

The *in-situ* mechanical evolution, as illustrated in Figure 12, highlights a complex reinforcement trajectory characterized by rapid early-stage response and site-specific long-term enhancement. During the initial 24-h treatment window, all monitoring points exhibited a synchronized and progressive increase in Leeb hardness (Figure 12a). Specifically, the mean hardness values advanced from their respective baselines (186–255 HL) to 234–326 HL by the 24th hour. This stage is dominated by relatively uniform kinetics across different application modes, where the rapid evaporation of the alcoholic carrier and the initial carbonation of $Ca(OH)_2$ nanoparticles effectively consolidate the immediate surface layer of the sandstone. The linear-like growth observed in Point 3 and Point 4 during this period underscores the high reactivity of the nanolime within the fractured and porous matrix.

A follow-up assessment conducted 100 days post-application revealed a significant divergence in mechanical performance, reflecting the long-term influence of micro-environmental conditions and application strategies. As shown in the boxplot distribution, Point 1, Point 2, and Point 5 attained a state of stabilization, with their hardness values (means of 243, 255, and 307 HL, respectively) remaining consistent with or slightly exceeding

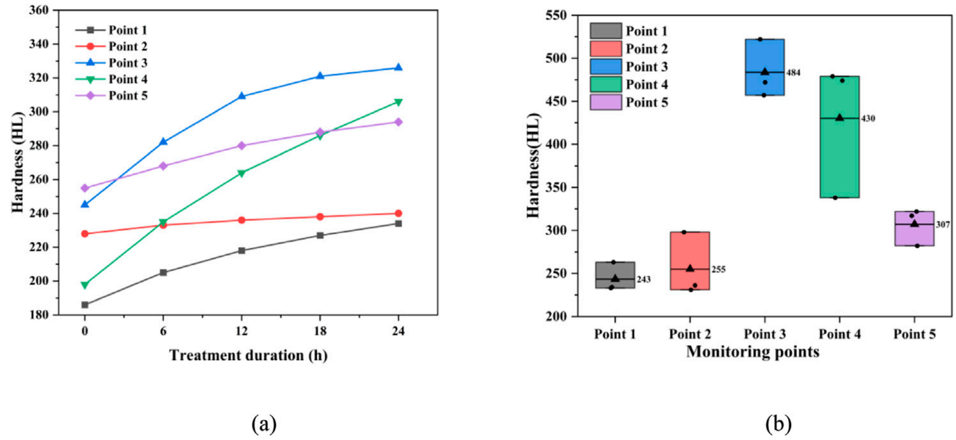

FIGURE 12
In-situ mechanical reinforcement performance of nanolime-treated sandstone at the Dazu Rock Carvings: **(a)** short-term reinforcement kinetics within the initial 24-h treatment; **(b)** long-term hardness distribution after 100 days.

their 24-h levels (Figure 12b). In stark contrast, Point 3 and Point 4 exhibited an extraordinary leap in mechanical strength, reaching mean values of 484 HL and 430 HL. This late-stage increment, particularly in the large-fracture zone (Point 3) and the shaded micro-pore zone (Point 4), is consistent with continued carbonation and progressive bonding after the initial drying phase, although site heterogeneity should also be considered. Furthermore, the 100-day data display increased dispersion, especially for Point 4, which is indicative of the intrinsic mineralogical heterogeneity of the heritage substrate and the non-uniform formation of a dense calcite network over time. These results confirm that while the nanolime provides immediate structural stabilization within the first diurnal cycle, its full reinforcement potential is realized through prolonged carbonation, leading to substantial and durable mechanical gains in specific high-deterioration zones.

The superior efficacy of the anion-exchange nanolime is likely associated with its nanoscale dimensions (50–100 nm) and the low surface tension of the isopropanol carrier. Compared with traditional limewater, whose consolidation effect is constrained by the low solubility of $Ca(OH)_2$ in water, approximately 1.7 g/L at room temperature, and the resulting limited calcium supply, the nanolime suspension provides a higher amount of reactive calcium hydroxide particles that can be transported into the pore-crack system of weathered sandstone. In addition, the nanoscale particles are more favorable for penetration into fine capillary pores and intergranular microcracks, whereas micron-sized lime particles or precipitates from traditional limewater are more prone to filtration and accumulation near the surface. This difference helps explain why the nanolime-treated specimens showed more effective mechanical improvement while maintaining acceptable porosity and permeability. During solvent evaporation, the meniscus effect may drive the preferential migration of hexagonal $Ca(OH)_2$ platelets toward narrow pore regions, particularly the intergranular contact points between quartz and feldspar (Sambudi and Biomineralization, 2017; Alam, 2015; Cramer et al., 2008). Consequently, $Ca(OH)_2$ nanoparticles deposit at these boundaries rather than occluding the central voids (Yakymechko et al., 2025). Upon carbonation, these localized deposits may form calcite-rich bonding zones that help restore mechanical cohesion while maintaining the stone's hydraulic continuity and breathability (Figure 13) (Alam, 2015). In contrast, the weaker response of traditional limewater under the same experimental conditions suggests that insufficient calcium hydroxide availability and less efficient pore-scale deposition limit its ability to form effective bonding zones within the weathered sandstone matrix. Therefore, the advantage of the anion-exchange nanolime treatment lies not only in its higher reinforcement efficiency, but also in its ability to achieve targeted pore-scale consolidation with reduced risk of pore blockage, moisture entrapment, and associated secondary deterioration.

The hydro-physical and aesthetic compatibility observed in the present study should also be interpreted in relation to the substrate-dependent responses reported in previous nanolime studies. Pozo-Antonio et al. (Pozo-Antonio et al., 2019) found that commercial Nanorestore reduced the open porosity of thermally damaged granite from 6.49% ± 0.53% to 4.60% ± 0.74%, corresponding to a reduction of approximately 29%, whereas its effect was much less favorable in fine-pored limestone, where porosity slightly increased from 2.32% ± 0.37% to 2.57% ± 0.48%. Barnoos et al. (Barnoos et al., 2022) further showed that, in extremely low-porosity limestone from the Anahita Temple, nanolime accumulated near the surface, increased porosity and free water absorption, and failed to improve freeze–thaw resistance. These results indicate that nanolime consolidation does not necessarily lead to compatible reinforcement when particle transport is restricted by an unsuitable pore structure. In contrast, the Dazu sandstone showed only a negligible porosity decrease after nanolime treatment, from 14.5% to 14.4%, corresponding to a relative reduction of 0.69%, and its gas permeability decreased by only 1.8%, from 5.5 to 5.4 mD. This limited change is much smaller than the pore refinement reported in several mortar or stone substrates, such as the porosity reduction from 23.34% ± 0.34% to 17.87% ± 0.71% reported by Otero et al. (Otero et al., 2020) and the concentration-dependent superficial porosity decrease from 31% ± 6% to 15% ± 4% reported by Taglieri

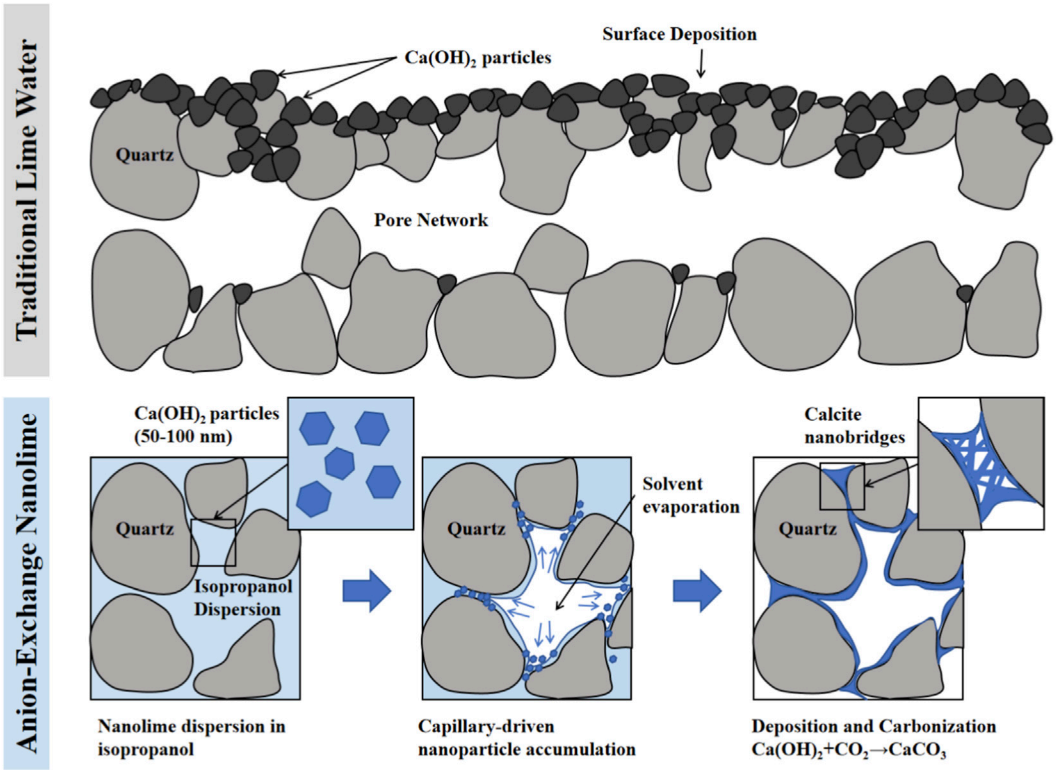

FIGURE 13
Schematic comparison of consolidation mechanisms between traditional lime water and anion-exchange synthesized nanolime for sandstone protection.

et al. (Taglieri et al., 2017b). In terms of visual compatibility, the mean color difference of the nanolime-treated Dazu sandstone was only ΔE_{ab} = 0.87–0.88, close to that of the traditional lime-water treatment (ΔE_{ab} = 0.66) and far below the visible whitening reported in some optimized nanolime systems, such as ΔE = 8.29 for CaLoSiL E90H10 (Busschots et al., 2025) and ΔE = 10.35 for a water–isopropanol nanolime suspension (Otero et al., 2020). Therefore, compared with these reported cases, the present anion-exchange nanolime achieved a more favorable balance between pore preservation and aesthetic neutrality, suggesting that the selected particle size, concentration, and isopropanol carrier were well matched to the connected pore-crack network of the weathered Dazu sandstone. The reinforcement effect is therefore more reasonably attributed to localized calcium carbonate-mediated bonding at intergranular contacts and microcrack interfaces rather than to large-scale pore filling or surface film formation.

Therefore, the main advantage of nanolime treatment under aging conditions lies not only in its initial strengthening effect, but also in its ability to delay the development of localized weak zones during environmental deterioration. The lower dispersion of nanoindentation data and the more continuous hardness/modulus maps indicate that nanolime forms a more stable reinforced layer under cyclic moisture and salt stresses. From a practical conservation perspective, this treatment should be regarded as a site-adapted consolidation strategy rather than a universal stone binder. Brushing was selected because it is minimally invasive and suitable for exposed sandstone surfaces, but its effectiveness may vary with surface roughness, crack openness, moisture condition, and weathering degree. For larger applications, batch-to-batch verification and preliminary trials on representative weathered zones are necessary, especially to control particle size, concentration, residual ions, and solvent safety. Periodic monitoring of color change, surface hardness, moisture transport, and visible deterioration is still required, and retreatment may be needed in zones affected by severe rainfall, salt migration, or repeated wetting–drying cycles.

5 Conclusion

In this study, an anti-weathering consolidation strategy for sandstone at the Dazu Rock Carvings was investigated. High-purity nanolime was synthesized using a one-step anion-exchange method, and its compatibility, mechanical reinforcement effect, aging resistance, and field applicability were systematically evaluated through laboratory tests and *in-situ* validation. The main conclusions are as follows:

1. The anion-exchange method successfully yields hexagonal portlandite nanoplates (50–100 nm) characterized by high

crystallinity and colloidal stability. This synthesis route substantially reduces chloride residues, with the residual Cl^- concentration decreasing to 0.11 g/L. Although no chloride-based crystalline by-products were detected by XRD, the possible long-term influence of residual chloride and any trace impurities from the resin should be evaluated in future durability studies.

2. The nanolime treatment preserves the hydro-physical equilibrium of the sandstone. Experimental evidence confirms that the total color difference (ΔE^*_{ab}) remains below the human perception threshold, while the alterations in open porosity and water permeability are strictly constrained within 5%. These results ensure that the treatment achieves aesthetic neutrality without jeopardizing the intrinsic breathability or vapor exchange capacity of the stone matrix.
3. The treatment is consistent with the formation of localized calcite bonding within the stone's pore structure, yielding a 25.8% increment in UCS. Micro-mechanical mapping through nanoindentation further elucidates the formation of a homogeneous reinforcement layer. Within this layer, the enhanced hardness and Young's modulus provide resistance against micro-structural fragility, effectively mitigating disintegration kinetics even after simulated hygrothermal-salt aging.
4. Field validation at the Beishan site of the Dazu Rock Carvings underscores the practical feasibility of the treatment across diverse decay morphologies. The *in-situ* monitoring captures a rapid mechanical recovery within the initial 24 h (rising from 186 to 255 HL to 234–326 HL). Subsequent follow-up at 100 days reveals a prolonged carbonation trajectory, particularly in highly weathered zones where surface hardness reaches 484 HL, confirming that the nanolime facilitates durable and site-specific mechanical gains.

Future work should include direct cross-sectional characterization of penetration depth and carbonation products, repeated synthesis batches to quantify batch-to-batch variability, longer-term field monitoring with untreated control areas, and systematic testing of carrier composition, application-cycle number and environmental exposure conditions.

Data availability statement

The original contributions presented in the study are included in the article/supplementary material, further inquiries can be directed to the corresponding author.

Author contributions

ZH: Writing – original draft. SW: Writing – review and editing. WZ: Writing – review and editing, Funding acquisition, Supervision, Resources, Methodology. AG: Data curation, Writing – review and editing, Formal Analysis. BM: Writing – review and editing, Investigation. YZ: Writing – review and editing, Validation. YC: Resources, Writing – review and editing.

Funding

The author(s) declared that financial support was received for this work and/or its publication. The authors are grateful to the financial supports from the National Natural Science Foundation of China (No. 52478325), Chongqing Natural Science Foundation Innovation and Development Joint Funding (CSTB2022NSCQ-LZX0001), Chongqing Municipal Research Institutions Performance Incentive and Guidance Special Project (CSTB2024JXJL-YFX0045), as well as the support from Helan Mountain Rock Art Management Office and Ningxia Donglai Energy Company.

Conflict of interest

The author(s) declared that this work was conducted in the absence of any commercial or financial relationships that could be construed as a potential conflict of interest.

Generative AI statement

The author(s) declared that generative AI was not used in the creation of this manuscript.

Any alternative text (alt text) provided alongside figures in this article has been generated by Frontiers with the support of artificial intelligence and reasonable efforts have been made to ensure accuracy, including review by the authors wherever possible. If you identify any issues, please contact us.

References

Alam, P. (2015). "Mechanical properties of bio-nanostructured materials," in *Handbook of Mechanical Nanostructuring*, 211–233.

Aslan, F., Arslan, M., and Eflatun, A. (2001). The solubility of calcium at stone monuments by acid rain. *Fresenius Environ. Bull.* 10 (3), 314–318.

Barnoos, V., Shekofteh, A., and Oudbashi, O. (2022). Experimental evaluation of the consolidation treatments of low porosity limestone from the historic monument of the Anahita Temple of Kangavar, Iran. *Archaeol. Anthropol. Sci.* 14 (4), 63. doi: 10.1007/s12520-022-01536-z

Busschots, E., De Kock, T., Berto, T., Peeters, K., Godts, S., and Fontaine, L. (2025). Consolidating lime mortar with nanolime: the effect of the ethanol: water ratio. *Stud. Conserv.* 70 (5), 358–366. doi: 10.1080/00393630.2024.2390271

Cramer, T., Zerbetto, F., and García, R. (2008). Molecular mechanism of water bridge buildup: field-induced formation of nanoscale menisci. *Langmuir.* 24 (12), 6116–6120. doi: 10.1021/la800220r

Cultrone, G., Sebastián, E., and Huertas, M. (2007). Durability of masonry systems:: a laboratory study. *Constr. Build. Mater.* 21 (1), 40–51. doi: 10.1016/j.conbuildmat.2005.07.008

Dai, S. B., Wang, J. H., Hu, Y., and Zhang, D. B. (2010). Lime-based materials and practices for surface refitting of cultural heritage. *Adv. Mater. Res.* 133, 1241–1246. doi: 10.4028/www.scientific.net/amr.133-134.1241

Dai, Z., Zhan, C., Dong, S., Yin, S., Zhang, X., and Soltanian, M. R. (2020). How does resolution of sedimentary architecture data affect plume dispersion in multiscale and hierarchical systems? *J. Hydrol.* 582, 124516. doi: 10.1016/j.jhydrol.2019.124516

Daniele, V., and Taglieri, G. (2012). Synthesis of Ca (OH) 2 nanoparticles with the addition of Triton X-100. Protective treatments on natural stones: preliminary results. *J. Cult. Herit.* 13 (1), 40–46. doi: 10.1016/j.culher.2011.05.007

De Matos, P. R., Neto, J. S. A., Sakata, R. D., Kirchheim, A., Rodríguez, E., and Campos, C. (2022). Strategies for XRD quantitative phase analysis of ordinary and blended Portland cements. *Cem. Concr. Compos.* 131, 104571. doi: 10.1016/j.cemconcomp.2022.104571

Dehestani, A., Hosseini, M., and Beydokhti, A. T. (2020). Effect of wetting–drying cycles on mode I and mode II fracture toughness of sandstone in natural (pH = 7) and acidic (pH = 3) environments. *Theor. Appl. Fract. Mech.* 107, 102512. doi: 10.1016/j.tafmec.2020.102512

Del Re, G. (2015). A new and original method to produce Ca (OH) 2 nanoparticles by using an anion exchange resin. *Adv. Nanoparticles* 4, 17–24. doi: 10.4236/anp.2015.42003

Goudie, A., and Viles, H. (1997). *Salt Weathering Hazards*.

Guo, X., Zhang, Y., Hao, R., Zhang, R., Cheng, Y., and Huang, J. (2025). Petrophysical and mechanical characterization of sandstones from different grottoes in China. *Herit. Sci.* 13 (1), 481. doi: 10.1038/s40494-025-02046-6

Guo, P., Miao, M., Zhao, H., Zuo, T., Wang, N., Yan, L., et al. (2026). Global divergent responses of soil heterotrophic respiration to nitrogen deposition. *CATENA* 269, 110117. doi: 10.1016/j.catena.2026.110117

Gupta, I., Sondergeld, C., and Rai, C. (2020). Fracture toughness in shales using nano-indentation. *J. Petroleum Sci. Eng.* 191, 107222. doi: 10.1016/j.petrol.2020.107222

Han, P., Zhang, H., Zhang, R., Tan, X., Zhao, L., Liang, Y., et al. (2022). Evaluation of the effectiveness and compatibility of nanolime for the consolidation of earthen-based murals at Mogao Grottoes. *J. Cult. Herit.* 58, 266–273. doi: 10.1016/j.culher.2022.10.017

Hanna, S., Price, C. A., Baer, N. S., and Snethlage, R. (1998). Stone conservation: an overview of current research. *Stud. Conserv.* 43 (2), 125–127. doi: 10.2307/1506649

He, X., Xu, M., Zhang, H., Zhang, B., and Su, B. (2014). An exploratory study of the deterioration mechanism of ancient wall-paintings based on thermal and moisture expansion property analysis. *J. Archaeol. Sci.* 42, 194–200. doi: 10.1016/j.jas.2013.10.035

Hong, Y., Wang, X., Wang, L., Kang, G., and Gao, Z. (2024). High-cycle shakedown, ratcheting and liquefaction behavior of anisotropic granular material with fabric evolution: experiments and constitutive modelling. *J. Mech. Phys. Solids.* 187, 105638. doi: 10.1016/j.jmps.2024.105638

İnce, İ., and Fener, M. (2016). A prediction model for uniaxial compressive strength of deteriorated pyroclastic rocks due to freeze–thaw cycle. *J. Afr. Earth. Sci.* 120, 134–140. doi: 10.1016/j.jafrearsci.2016.05.001

Jiahang, S., Shaojun, Y., Wei, X., Jianhui, L., Gang, Z., and Siwei, J. (2022). Influencing factors of capillary water migration characteristics of the sandstones in Baoding Mountain, Dazu Stone Carvings. *Geol. Sci. Technol. Inf.* 41 (4), 282–291. doi: 10.19509/j.cnki.dzkq.2021.0099

Khanlari, G., and Abdilor, Y. (2015). Influence of wet–dry, freeze–thaw, and heat–cool cycles on the physical and mechanical properties of Upper Red sandstones in central Iran. *Bull. Eng. Geol. Environ.* 74 (4), 1287–1300. doi: 10.1007/s10064-014-0691-8

Lanas, J., and Alvarez, J. (2003). Masonry repair lime-based mortars: factors affecting the mechanical behavior. *Cem. Concr. Res.* 33 (11), 1867–1876. doi: 10.1016/s0008-8846(03)00210-2

Li, L., Chen, J., Gao, C., Zhou, Z., Li, M., Zhang, D., et al. (2025). Peridynamics simulation of hydraulic fracturing in three-dimensional fractured rock mass. *Phys. Fluids.* 37 (7), 073628. doi: 10.1063/5.0274871

Lin, S., Wang, L., Zhang, W., Wang, S., Zhang, K., Lei, Y., et al. (2024). Cross-scale quantitative and qualitative study of grotto sandstone under salt weathering. *Rock Mech. Rock Eng.* 57 (12), 10953–10971. doi: 10.1007/s00603-024-04130-y

Liu, K., Ostadhassan, M., and Bubach, B. (2016). Applications of nano-indentation methods to estimate nanoscale mechanical properties of shale reservoir rocks. *J. Nat. Gas. Sci. Eng.* 35, 1310–1319. doi: 10.1016/j.jngse.2016.09.068

Liu, Y., Cheng, P., Zeng, T., Wang, Y., Xie, S., and Wu, L. (2026a). Reconstruction of vegetation-occluded rock point clouds for discontinuity identification. *Eng. Geol.* 367, 108726. doi: 10.1016/j.enggeo.2026.108726

Liu, G., Luo, S., Zhang, S., Ma, K., Bo, W., Fan, H., et al. (2026b). Experimental verifications and applications of discontinuous deformation analysis in block-type rock slope failure and movement mechanisms. *Rock Mech. Rock Eng.* doi: 10.1007/s00603-026-05557-1

Miller, L. B., and Witt, J. C. (2002). Solubility of calcium hydroxide. *J. Phys. Chem.* 33 (2), 285–289. doi: 10.1021/j150296a010

Mudronja, D., Vanmeert, F., Fazinic, S., Janssens, K., Tibljas, D., and Desnica, V. (2021). Protection of stone monuments using a brushing treatment with ammonium oxalate. *Coatings* 11 (4), 379. doi: 10.3390/coatings11040379

Onofri, S., Zucconi, L., Isola, D., and Selbmann, L. (2014). Rock-inhabiting fungi and their role in deterioration of stone monuments in the Mediterranean area. *Plant Biosyst.* 148 (2), 384–391. doi: 10.1080/11263504.2013.877533

Otero, J., Starinieri, V., and Charola, A. E. (2018). Nanolime for the consolidation of lime mortars: a comparison of three available products. *Constr. Build. Mater.* 181, 394–407. doi: 10.1016/j.conbuildmat.2018.06.055

Otero, J., Starinieri, V., Charola, A. E., and Taglieri, G. (2020). Influence of different types of solvent on the effectiveness of nanolime treatments on highly porous mortar substrates. *Constr. Build. Mater.* 230, 117112. doi: 10.1016/j.conbuildmat.2019.117112

Parvin, N., Mandal, S., and Rath, J. (2024). Microbiome of seventh-century old Parsurameswara stone monument of India and role of desiccation-tolerant cyanobacterium Lyngbya corticicola on its biodeterioration. *Biofouling* 40 (1), 40–53. doi: 10.1080/08927014.2024.2305381

Pope, C. G. (1997). X-ray diffraction and the Bragg equation. *J. Chemical Education* 74 (1), 129. doi: 10.1021/ed074p129

Pozo-Antonio, J. S., Otero, J., Alonso, P., and Mas i Barberà, X. (2019). Nanolime-and nanosilica-based consolidants applied on heated granite and limestone: effectiveness and durability. *Constr. Build. Mater.* 201, 852–870. doi: 10.1016/j.conbuildmat.2018.12.213

Ren, Q., Liu, T., Wan, D., Wang, J., Jiang, R., Li, M., et al. (2026). An innovative approach to discrete facture network modeling driven by geomechanics and multiple factors. *Geoenergy Sci. Eng.* 257, 214200. doi: 10.1016/j.geoen.2025.214200

Rodriguez-Navarro, C., Suzuki, A., and Ruiz-Agudo, E. (2013). Alcohol dispersions of calcium hydroxide nanoparticles for stone conservation. *Langmuir.* 29 (36), 11457–11470. doi: 10.1021/la4017728

Sambudi, N. S., and Biomineralization, S. P. C. (2017). *An Inspiration from Nature for the Synthesis of Advanced Materials*. New York, NY: Nova Science Publishers, Inc., 1–17.

Schuster, P. F., Reddy, M. M., and Sherwood, S. I. (1994). Effects of acid-rain and sulfur-dioxide on marble dissolution. *Mater. Perform.* 33 (1), 76–80.

Skoulikidis, T., Vassiliou, P., and Tsakona, K. (2005). Surface consolidation of pentelic marble: criteria for the selection of methods and materials-the acropolis case (6 pp). *Environ. Sci. Pollut. Res.* 12 (1), 28–33. doi: 10.1065/espr2004.11.230

Smith, B. J., Srinivasan, S., Gomez-Heras, M., Basheer, P., and Viles, H. (2011). Near-surface temperature cycling of stone and its implications for scales of surface deterioration. *Geomorphology* 130 (1), 76–82. doi: 10.1016/j.geomorph.2010.10.005

Stepkowska, E., Perez-Rodriguez, J., De Haro, M., and Sayagues, M. J. (2002). Study of hydration of two cements of different strengths. *J. Therm. Analysis Calorim.* 69 (1), 187–204. doi: 10.1023/a:1019902210255

Sun, B. (2024). Niches and sculptures of the imaginary realm-revisiting the Fowan rock carvings, Beishan, dazu. *Religions* 15 (1), 50. doi: 10.3390/rel15010050

Taglieri, G., Felice, B., Daniele, V., Volpe, R., and Mondelli, C. (2016). Analysis of the carbonatation process of nanosized Ca (OH) 2 particles synthesized by exchange ion process. *Proc. Inst. Mech. Eng. Part N. J. Nanomater. Nanoeng. Nanosyst.* 230 (1), 25–31. doi: 10.1177/1740349914537616

Taglieri, G., Daniele, V., Macera, L., and Mondelli, C. (2017a). Nano Ca (OH) 2 synthesis using a cost-effective and innovative method: reactivity study. *J. Am. Ceram. Soc.* 100 (12), 5766–5778. doi: 10.1111/jace.15112

Taglieri, G., Daniele, V., Rosatelli, G., Sfarra, S., Mascolo, M. C., and Mondelli, C. (2017b). Eco-compatible protective treatments on an Italian historic mortar (XIV century). *J. Cult. Herit.* 25, 135–141. doi: 10.1016/j.culher.2016.12.008

Taglieri, G., Daniele, V., and Macera, L. (2019). Synthesizing alkaline earth metal hydroxides nanoparticles through an innovative, single-step and eco-friendly method. *Solid State Phenom.* 286, 3–14. doi: 10.4028/www.scientific.net/ssp.286.3

Tang, Y., Shao, Z., and Xu, T. (2018). Uniaxial compressive tests on ancient brick masonry from heritage buildings under unsaturated freeze-thaw conditions. *Constr. Build. Mater.* 183, 706–715. doi: 10.1016/j.conbuildmat.2018.06.157

Wang, Y., and Hua, P. (1998). The environment, composition, and protection of Dazu rock inscriptions. *Environ. Geol.* 33 (4), 295–298. doi: 10.1007/s002540050249

Wang, F., Huang, J., and Zhao, H. (2023). Mechanical sandstone deterioration due to cement binder material materials under dry-wet cycling. *Case Stud. Constr. Mater.* 18, e02169. doi: 10.1016/j.cscm.2023.e02169

Wang, S., Zhang, W., Zhang, Y., Lin, S., Sun, W., Jiang, S., et al. (2025a). Dynamic mechanical behavior and failure evolution of water-bearing grotto sandstone under cyclic loading and unloading. *Eng. Fract. Mech.* 328, 111573. doi: 10.1016/j.engfracmech.2025.111573

Wang, S., Wang, L., Zhang, W., Lin, S., Sun, W., Jiang, S., et al. (2025b). Microstructural deterioration mechanism and failure mode of water-immersed sandstone under uniaxial compression in Dazu rock carvings. *Eng. Fract. Mech.* 321, 111110. doi: 10.1016/j.engfracmech.2025.111110

Wang, L., Hao, Q., Zhong, Y., Liu, X., Xie, Q., Tian, X., et al. (2026). Influence of native pores on the size distribution and predictability of rock failure. *J. Rock Mech. Geotech. Eng.* 18 (2), 1447–1459. doi: 10.1016/j.jrmge.2025.12.009

Wu, M., Ma, Z., He, Z., Ding, J., Zhao, X., Ruiz-Agudo, E., et al. (2026). Consolidating tomb mural plaster layer with nanolime. *J. Cult. Herit.* 77, 7–14. doi: 10.1016/j.culher.2025.10.014

Yakymechko, Y., Jaskulski, R., Jóźwiak-Niedźwiedzka, D., and Banach, M. (2025). Chemistry, technology and utilization of nanolime. *Materials.* 18 (21), 4846. doi: 10.3390/ma18214846

Yang, R., He, S., Liu, J., Shen, J., Wang, L., Yu, Y., et al. (2024). Tensile strength and failure mechanism of rock-cement sample: roles of curing temperature, nano-silica and rock type. *Cem. Concr. Res.* 186, 107673. doi: 10.1016/j.cemconres.2024.107673

Yang, P., Tao, Z., Yang, X., and Li, X. (2025). Roof deformation of the Beishan Rock Carvings with negative Poisson's ratio anchor support under varied precipitation conditions. *J. Mt. Sci.* 22 (8), 3078–3091. doi: 10.1007/s11629-024-9363-8

Zhang, J., Fang, Z., Zhang, X., Yu, Y., Wang, S., and Cao, Y. (2026). 3D fractal tortuosity quantification of impact-induced coal fractures: a permeability enhancement model for gas extraction. *Rock Mech. Rock Eng.* doi: 10.1007/s00603-026-05486-z

Zhao, Q., Liu, S., Yuan, W., Lu, Q., Tian, S., Ni, J., et al. (2024). Fracture system assess in Beishan Grottos, Chongqing, China based on multiple geophysical data. *IEEE Access* 12, 117665–117677. doi: 10.1109/access.2024.3438768

Zheng, Y., and Baudet, B. A. (2024). Evolution of nano-pores in illite-dominant clay during consolidation. *Acta Geotech.* 19 (1), 71–83. doi: 10.1007/s11440-023-02014-z

Zheng, Y., Coop, M. R., Tang, H., and Fan, Z. (2022). Effects of overconsolidation on the reactivated residual strength of remoulded deep-seated sliding zone soil in the three Gorges Reservoir Region, China. *Eng. Geol.* 310, 106882. doi: 10.1016/j.enggeo.2022.106882

Zheng, Y., Baudet, B. A., Delage, P., Pereira, J. M., and Sammonds, P. (2023). Pore changes in an illitic clay during one-dimensional compression. *Geotechnique* 73 (10), 917–932. doi: 10.1680/jgeot.21.00206